Strong Photocurrent Enhancements in Plasmonic Organic Photovoltaics by Biomimetic Nanoarchitectures with Efficient Light Harvesting

Jung Woo Leem,[†,§] Sehwan Kim,[‡,§] Chihyun Park,[‡] Eunkyoung Kim,*[‡] and Jae Su Yu*[†]

[†]Department of Electronics and Radio Engineering, Kyung Hee University, 1732 Deogyeong-daero, Giheung-gu, Yongin-si, Gyeonggi-do 446-701, Republic of Korea

[‡]Department of Chemical and Biomolecular Engineering, Yonsei University, 50 Yonsei-ro, Seodaemun-gu, Seoul 120-749, Republic of Korea

Ⓢ Supporting Information

ABSTRACT: We propose the biomimetic moth-eye nanoarchitectures as a novel plasmonic light-harvesting structure for further enhancing the solar-generated photocurrents in organic photovoltaics (OPVs). The full moth-eye nanoarchitectures are composed of two-dimensional hexagonal periodic grating arrays on surfaces of both the front zinc oxide (ZnO) and rear active layers, which are prepared by a simple and cost-effective soft imprint nanopatterning technique. For the 380 nm period ZnO and 650 nm period active gratings (i.e., ZnO(P380)/Active(P650)), the poly(3-hexylthiophene-2,5-diyl):in-dene-C_{60} bis-adduct (P3HT:ICBA)-based plasmonic OPVs exhibit an improvement of the absorption spectrum compared to the pristine OPVs over a broad wavelength range of 350−750 nm, showing absorption enhancement peaks at wavelengths of ~370, 450, and 670 nm, respectively. This leads to a considerable increase of short-circuit current density (J_{sc}) from 10.9 to 13.32 mA/cm², showing a large J_{sc} enhancement percentage of ~22.2%. As a result, the strongly improved power conversion efficiency (PCE) of 6.28% is obtained compared to that (i.e., PCE = 5.12%) of the pristine OPVs. For the angle-dependent light-absorption characteristics, the plasmonic OPVs with ZnO(P380)/Active(P650) have a better absorption performance than that of the pristine OPVs at incident angles of 20−70°. For optical absorption characteristics and near-field intensity distributions of plasmonic OPVs, theoretical analyses are also performed by a rigorous coupled-wave analysis method, which gives a similar tendency with the experimentally measured data.

KEYWORDS: organic photovoltaics, moth-eye gratings, light harvesting, plasmonic effect, soft imprint nanopatterning
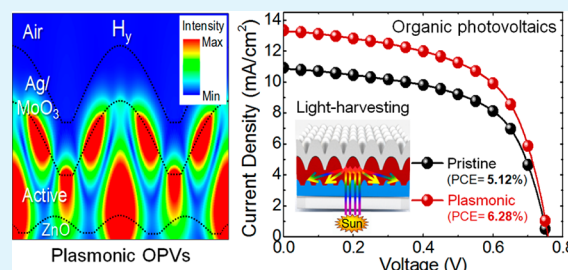
1. INTRODUCTION

Development of thin film-based photovoltaic (PV) cells grown on inexpensive substrates (i.e., glasses and polymers) is considered as one of the most promising strategies to reduce the cost of solar power generation for a wide range of potential applications from windows and claddings for building-integrated PV generation to automotive and portable power sources.[1−3] Especially, organic photovoltaics (OPVs) have attracted enormous attention as one of the most promising alternative renewable energy sources because of their light-weight, high throughput, conformability, and low-temperature facile solution processability.[4,5] The recent progress in achieving solar power conversion efficiencies (PCEs) surpassing 10% of OPVs is a milestone in fields of solar energy devices for prospects of commercialization.[1,5] Ideally, a photoactive layer in OPVs should be sufficiently thick to absorb most of the incoming sunlight. However, the quantum efficiency of OPVs with thicker photoactive layers is still limited by the comparatively low carrier mobility, which may cause charge-recombination losses.[6,7] Therefore, it is necessary to increase the PCE of OPVs with a limited photoactive layer thickness in

an effective light-harvesting way including light-trapping and photon-management techniques in the photoactive region. In this respect, recently, several concepts have been studied on thickness optimizations of thin film,[8,9] grating structures by nanopatterning techniques,[10−17] surface treatment by additives,[18,19] textured surface structures as antireflection coatings,[13,20] and localized surface plasmons using metallic nanoparticles and quantum dots.[21−23] Among these approaches, particularly, using simple, inexpensive, and large-scalable soft imprint nanopatterning techniques, periodic grating structures at the front (i.e., zinc oxide (ZnO)/active layer) or rear (i.e., active/metal layer) electrode of OPVs lead to reduced reflection losses and enhanced optical path lengths by scattering and diffraction of lights reflected from the rear metal layer in the device over a wide wavelength range of solar spectrum and thus effectively enhance the light absorption in the active layer, resulting in the PCE improvement of
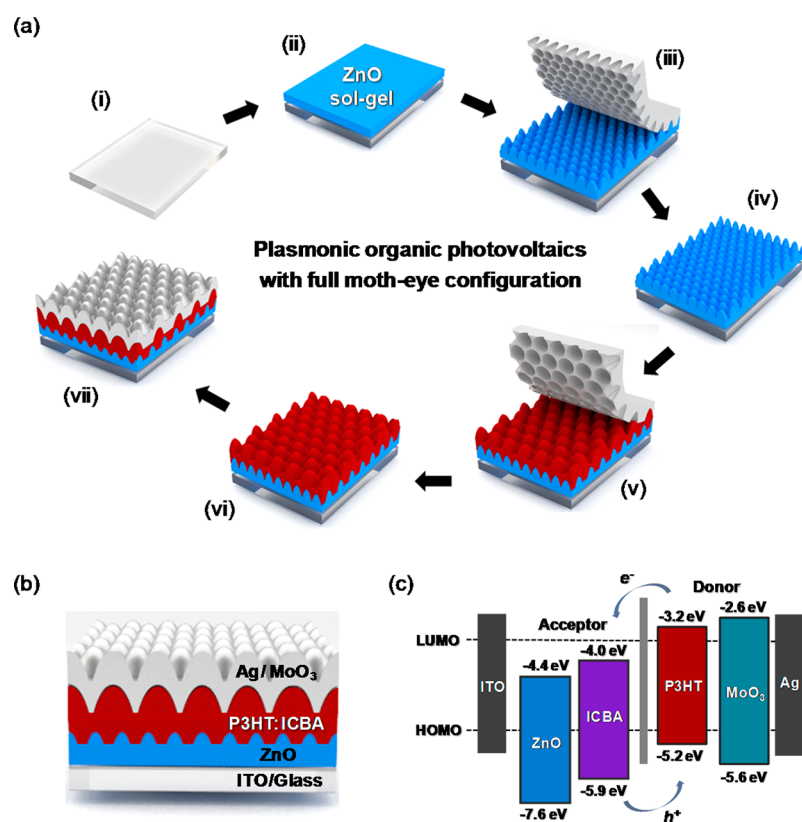
Figure 1. (a) Schematic of the fabrication sequence for plasmonic OPVs with a full moth-eye configuration: (i) Preparation of ITO substrates, (ii) spin coating of sol−gel derived ZnO precursor layers, (iii) nanopatterning process of ZnO layers via PDMS stamps, (iv) moth-eye architecture on ZnO layers, (v) nanopatterning process of photoactive layers via PDMS stamps, (vi) moth-eye architecture of photoactive layers, (vii) thermal evaporation of MoO_3 with Ag electrodes on active layers, (b) cross-sectional view of OPV device architecture, and (c) cascade energy level diagram of constituent materials in OPVs including the HOMO and LUMO energies.

OPVs.[10−17] In addition, these nanopatterned OPVs at inside layers can contribute to more effective carrier transport because of the increase of the interfacial area.[24−26] Besides, the nanoscale grating structures at the interface between the photoactive and rear metal layers produce strong electromagnetic fields, that is, surface plasmon resonances (SPRs), which can increase photocurrents in the active layer of OPVs at some wavelengths.[11−13] Also, the OPVs with biomimetic moth-eye corneal nipple structures, which consist of two-dimensional (2D) periodic grating arrays at the rear electrode, show a better device performance than ones with one-dimensional (1D) line grating patterns.[10] Optical properties (e.g., transmission, reflection, diffraction, etc.) of the light strongly depend on the period of grating structures.[27−29] Thus, it is very meaningful to investigate the optical and device characteristics of OPVs by varying the period of gratings with 2D hexagonal pattern arrays. Although there are many studies on the PCE enhancement of OPVs with the 1D line or 2D grating patterns at the front or rear electrode,[10−13,25,26] very little or no work has been reported on the use of moth-eye architectures with 2D grating patterns at both the front and rear electrodes in OPVs for different periods, together with a theoretical analysis. In this work, we fabricated the poly(3-hexylthiophene-2,5-diyl):indene-C_{60} bis-adduct (P3HT:ICBA) photoactive material-based OPVs, which consist of ZnO/P3HT:ICBA/MoO_3/Ag structures, with full moth-eye grating architectures (i.e., both the front ZnO and rear P3HT:ICBA active layers) via a soft imprint nanopatterning. Their device performances with optical properties were investigated, including a long-term stability.

Using a rigorous coupled-wave analysis (RCWA) method, the effect of moth-eye gratings on near-field intensity distributions and the resulting enhanced optical absorbance in the plasmonic OPV structures were studied. The angle-dependent optical characteristics were also explored.

2. EXPERIMENTAL AND OPTICAL SIMULATION DETAILS

2.1. Materials and Methods. Figure 1 shows the (a) schematic illustration of the fabrication sequence for plasmonic OPVs with a full moth-eye configuration, (b) cross-sectional view of OPV device architecture, and (c) cascade energy level diagram of OPV constituent materials including the highest occupied molecular orbital (HOMO) and lowest unoccupied molecular orbital (LUMO) energies. As can be seen in Figure 1a, first, to fabricate the OPVs with moth-eye grating architectures, indium tin oxide (ITO)-coated glass substrates (13Ω/square, Samsung Corning Corp.), which were cleaned successively by ultrasonication in detergent, acetone, ethanol, and deionized water for 15 min and finally dried in an oven (110 °C) for 3 h, were used as a front electrode. The sol−gel-derived ZnO precursor, which was prepared by dissolving zinc acetate dihydrate ($Zn(C_2H_3O_2)_2$·$2H_2O$, i.e., $Zn(OAc)_2$·$2H_2O$, 220 mg, 0.5 M) and methanolamine (0.5 M) in 2-methoxyethanol ($CH_3OCH_2CH_2OH$, 2 mL) with vigorous stirring for 12 h for the hydrolysis reaction at ambient conditions,[30] with a thickness of ∼30 nm was spin-coated on the surface of ITO/glass substrates and sintered. Then, it was imprinted using the poly(dimethylsiloxane) (PDMS) stamps with negative grating arrays. PDMS stamps with four periods of 380, 500, 650, and 840 nm were prepared from silicon (Si) master molds with conical gratings consisting of 2D periodic hexagonal patterns that were fabricated by laser interference lithography and dry etching processes. For both the
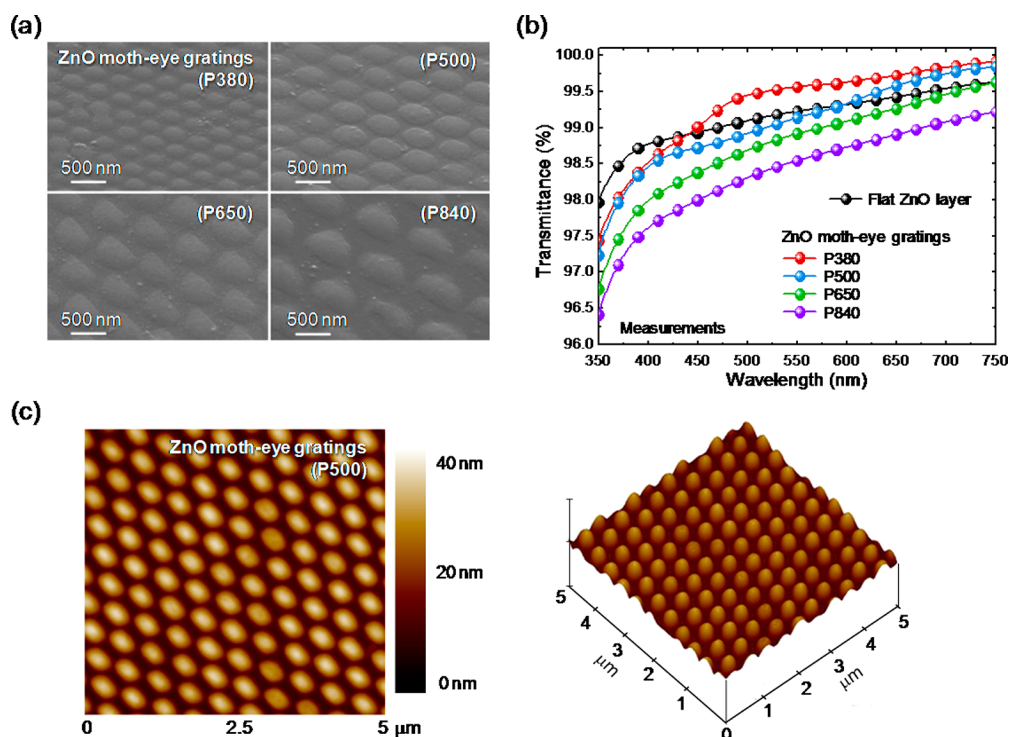
Figure 2. (a) 40°-tilted oblique-view SEM images and (b) measured transmittance spectra of ZnO moth-eye gratings for different periods (P) of 380, 500, 650, and 840 nm. (c) AFM image of the ZnO moth-eye gratings (P500). For comparison, the transmittance spectrum of flat ZnO layer is also shown in (b).

Si molds and PDMS stamps used in this experiment, the detailed fabrication method and information can be found in our previous works.[20,31] After detaching the PDMS stamps from the ZnO layer, the 200 nm thick P3HT:ICBA (RIEKE metals) photoactive layer was spin-coated on the top surface of the ZnO gratings/layer and subsequently imprinted by the PDMS stamps. Then, the thermal annealing was carried out at 85 °C for 10 min. After annealing, the PDMS stamps were carefully separated from the photoactive layer without cracks or any defects. Lastly, as a rear electrode, the molybdenum trioxide (MoO_3, 5 nm)/silver (Ag, 100 nm) layers were deposited on the samples by using a thermal evaporation system, respectively, under the interconnected high vacuum (8×10^{-7} Torr) with a shadow mask, and the device area (9 mm²) was defined as the active area of the corresponding OPVs, creating the plasmonic OPVs with a full moth-eye grating configuration, as shown in Figure 1b. In Figure 1c, the energy flow diagram exhibits the E_{LUMO} and E_{HOMO} values of polymers with each component. Herein, the ZnO layer acts as an electron (e^-)-transporting and hole-blocking layer in the device. The bound exciton (i.e., electron−hole pair) is generated by the incoming light, and then it is facilitated to be charge recombination and segregation at the interface of P3HT:ICBA-based interpenetrated percolating networks. Thus, electrons shift toward the front ITO electrode through the ZnO layer, and holes (h^+) move toward the rear Ag electrode.

2.2. Characterization of Samples. Structural and morphological properties of the fabricated samples were observed by using a scanning electron microscope (SEM; LEO SUPRA 55, Carl Zeiss) and focused ion-beam (FIB; Quanta 3D FEG, FEI) system. For the surface morphology of ZnO gratings, tapping-mode atomic force microscope (TM-AFM) analysis was carried out by tapping mode at room temperature with a Dimension 3100 SPM equipped with Nanoscope IV devised by Digital Instruments. The total reflectance and transmittance were measured by using a UV−vis−near-IR spectrophotometer (Cary 5000, Varian) with an integrating sphere at near normal incidence of ∼3°. A spectroscopic ellipsometry (V-VASE, J. A. Woollam) was used for the measurement of angle-dependent optical characteristics at incident angles of 20−70° in nonpolarized light and

for the characterization of refractive index and extinction coefficient of ZnO and active materials. Linearly polarized diode laser beam (intensity of 3.3 mW) with a wavelength (λ) of 635 nm was used as the probe light source for light-trapping experiment at incident angles of 15−60°. The incident laser ray is irradiated to a sample through the pinhole, and then the reflected zeroth-order ray is detected in the photodetector as a light intensity. Current density−bias voltage ($J−V$) curves were measured using a Keithley 2400 source measurement unit under illuminated conditions at an intensity of 100 mW/cm² using a 1 kW Oriel solar simulator with an air mass (AM) 1.5 G filter. For accurate measurements, the light intensity was calibrated using a radiant power meter and reference silicon solar cells certified by the National Renewable Energy Laboratory (NREL). Incident photon to current conversion efficiency (IPCE) spectra of devices were obtained using Oriel IQE 200 model, which combined monochromator and lock-in amplifier by comparison to a calibrated Si photodiode.

2.3. Theoretical Modeling and Calculations. Optical analyses (i.e., absorption, reflection, transmission, near fields) of plasmonic OPVs were performed using an RCWA method in a commercial software package (DiffractMOD, Rsoft Design Group). It was assumed that the incident light entered from air into the device at incident angles of 0−70°. To design the simulation models, gratings on both the ZnO and active layers were represented by a periodic geometry with a 2D hexagonal pattern in the Cartesian coordinate system by a scalar-valued function of three variables, $f(x,y,z)$, for simplicity. The shape of gratings can be defined by the following equations:[20]

$$r = R_{grating} \times [(H_{grating} - z)/H_{grating}]^{1/O_T} \text{ and } x^2 + y^2$$
$$= r^2 \ (0 \leq z \leq H_{grating}) \tag{1}$$

where the r is the radius of circle in xy plane, $H_{grating}$, $R_{grating}$, and O_T is the height, the bottom radius, and the order of taper of gratings, respectively. In calculations, the heights, orders of taper, and ratios of the bottom diameter of gratings to the period between gratings were kept at 30 and 130 nm, 1 and 1.5, and 0.8 and 0.8 for ZnO(P380) and Active(P650) gratings, respectively.
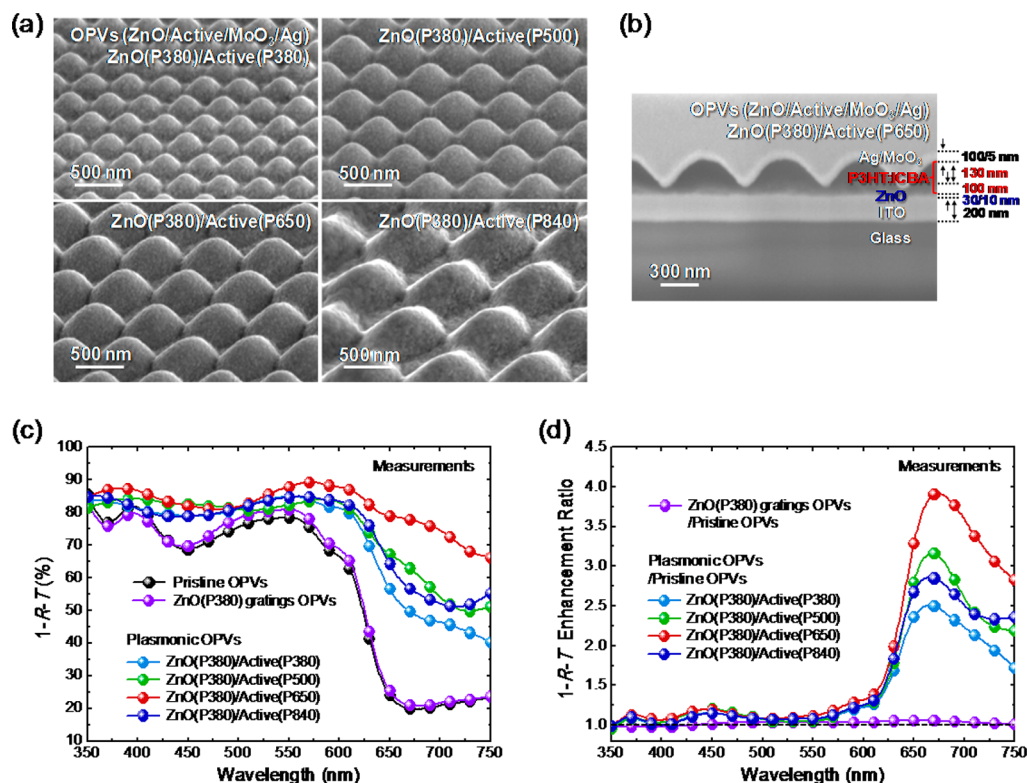
Figure 3. (a) 40°-tilted oblique-view SEM images of plasmonic OPVs with active gratings for different periods of 380, 500, 650, and 840 nm at the ZnO (P380) gratings. (b) Cross-sectional SEM image of plasmonic OPVs with ZnO(P380)/Active(P650). (c) 1-reflectance (R)-transmittance (T) (i.e., absorption) spectra of pristine OPVs, ZnO (P380) gratings OPVs, and the corresponding plasmonic OPVs. (d) Absorption enhancement ratio of ZnO (P380) gratings OPVs and plasmonic OPVs compared to the pristine OPVs.

3. RESULTS AND DISCUSSION

Figure 2 shows the (a) 40°-tilted oblique-view SEM images and (b) measured transmittance spectra of ZnO moth-eye gratings for different periods of 380, 500, 650, and 840 nm. In addition, the transmittance behavior of flat ZnO layer was demonstrated, as shown in Figure 2b. For the ZnO moth-eye gratings with a period of 500 nm (i.e., P500), topographic images were investigated by using a TM-AFM, as shown in Figure 2c. From both the SEM (Figure 2a) and AFM (Figure 2c) images, it can be observed that the moth-eye gratings with 2D periodic sixfold hexagonal pattern arrays were well-formed on the surfaces of imprinted ZnO layers by the PDMS stamps. For all the samples, the average height of ZnO gratings and the average thickness of remaining ZnO layers were approximately 30 nm and 10 nm, respectively. As shown in Figure 2b, the transmittance is strongly dependent on the period of ZnO moth-eye gratings. As the period is increased, the transmittance is gradually decreased. Also, it is observed that the transmittance spectra start to drop at wavelengths close to the grating periods, especially, for the samples with periods of 380 and 500 nm, because of their diffraction losses caused by higher-order diffracted waves.[29,32] This drop behavior can be also found in previous reports.[29,32−34] But, the diffraction losses are not large due to the very low height (i.e., ~30 nm) of gratings.[34] Nevertheless, the ZnO moth-eye gratings with a period of 380 nm (P380) exhibited a higher transmittance than that of the flat ZnO layer over a wide wavelength of 430−750 nm, which is attributed to the only allowed zeroth-order wave at wavelengths much higher than the period of 380 nm as well as the gradient effective refractive index profile via conical gratings, that is, "moth-eye effect".[35,36] Its solar weighted

transmittance (T_{sw}), which can be estimated by normalizing the measured transmittance spectrum with the solar spectral photon flux (i.e., AM1.5G[37]) integrated over a wavelength range of 350−750 nm,[38] of ~99.5% is higher than those of the other samples (i.e., $T_{sw} \approx$ 99, 98.9, and 98.5% for the ZnO moth-eye gratings with periods of 500, 650, and 840 nm, respectively) as well as the flat ZnO layer (i.e., $T_{sw} \approx$ 99.1%). Furthermore, the front electrode with gratings can enhance the trapping or scattering of reflected lights from the rear metal electrode in the active region of OPVs, which leads to the larger photocurrent.[26,39] Besides, the moth-eye gratings on the surface of ZnO layer can reduce the electron-transfer distance between the active layer and electrodes due to the increased interfacial surface area and thus decrease the exciton recombination losses.[24−26] Thus, the ZnO moth-eye gratings with a period of 380 nm can help to enhance the light harvesting and the travel of photogenerated carriers into electrodes compared to the flat ZnO layer in the active layer of OPVs.

Figure 3a shows the 40°-tilted oblique-view SEM images of plasmonic OPVs with active gratings for different periods of 380, 500, 650, and 840 nm at the ZnO (P380) gratings. As shown in Figure 3a, it can be observed that, using the PDMS stamps, the corrugated surface morphologies with 2D hexagonal periodic pattern arrays are well-formed on the imprinted active layer for different periods, resulting in the OPVs with a full moth-eye configuration (i.e., gratings on both the front ZnO and rear active layers). From the cross-sectional SEM image characterized by the FIB cutting in Figure 3b, for the plasmonic OPVs with 650 nm period active gratings (i.e., ZnO(P380)/Active(P650)), all the constituent materials are well-multistacked on the ITO/glass substrate. For the
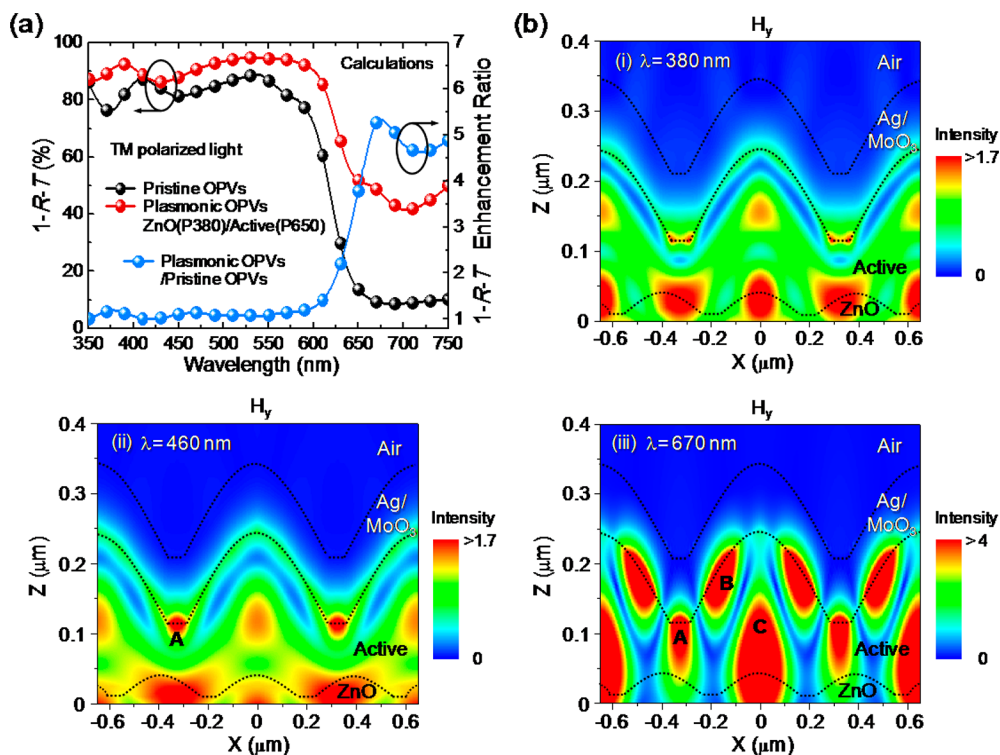
Figure 4. (a) Calculated absorption (1-R-T) spectra and enhancement ratio for pristine OPVs and plasmonic OPVs with ZnO(P380)/Active(P650) and (b) near-field intensity distributions in plasmonic OPVs with ZnO(P380)/Active(P650) at different wavelengths of (i) 380 nm, (ii) 460 nm, and (iii) 670 nm for TM polarized light.

imprinted gratings on the active layer, the average height was ~130 nm, and the average thickness of the remaining active layer was ~100 nm, respectively. As can be seen in Figure S1a (see the Supporting Information), the heights of the other plasmonic OPVs were estimated to be ~100, 120, and 150 nm for periods of 380, 500, and 840 nm, respectively, indicating remaining active layer thicknesses of ~120, 90, and 60 nm for the corresponding OPVs. Also, the uniformly well-ordered gratings on the surface of OPVs can be observed over a large area in the low-magnification SEM image of Figure S1b (see the Supporting Information). To investigate the light-trapping nature of OPVs with full moth-eye gratings, the absorption (i.e., 1-R-T) was extracted by the measured reflectance (R) and transmittance (T) (see Figure S2 of the Supporting Information). Figure 3c shows the extracted absorption (1-R-T) spectra of pristine OPVs, ZnO (P380) gratings OPVs, and plasmonic OPVs. Compared with the pristine OPVs, the absorption of OPVs with the only ZnO (P380) gratings was slightly increased. However, the introduction of gratings on the active layer into OPVs exhibited a further significant improvement on the absorption spectra over a wide wavelength range of 350−750 nm. For all the OPV devices, to explore the percentage of the absorbed solar energy in the active layer, the solar weighted absorption (A_{sw}) was also evaluated. The A_{sw} is given by the following equation[40]

$$A_{sw} = \frac{\int_{350nm}^{750nm} a(\lambda)S(\lambda)d\lambda}{\int_{350nm}^{750nm} S(\lambda)d\lambda} \qquad (2)$$

where $a(\lambda)$ is the absorption spectrum in Figure 3c and $S(\lambda)$ is the solar irradiance spectrum (i.e., AM1.5G). The plasmonic OPVs with ZnO(P380)/Active(P650) had a larger estimated

A_{sw} value of ~82% compared to those of the other plasmonic OPVs (i.e., $A_{sw} \approx$ 71.8, 75.2, and 74.5% at P380, P500, and P840, respectively, for the active gratings) and the pristine OPVs (i.e., $A_{sw} \approx$ 57.8%). To clarify the increased absorption of plasmonic OPVs compared to the pristine OPVs, an enhancement ratio was calculated in Figure 3d. Among the plasmonic OPVs with full moth-eye architectures, especially, the absorption enhancement of the device with ZnO(P380)/Active(650) is remarkable. This is ascribed to the enhanced light trapping caused by the increased transmittance and scattering effects of lights reflected from the rear metal layer as well as the improved photogenerated charge transport due to the larger interfacial surface area induced by gratings at both the ZnO and active layers.[11−13,24−26,39] When periodic gratings are provided on the active/metal layer in OPVs, incident light reaching the gratings can be diffracted in a backward direction.[13,14,41] The angle of the diffracted light can be determined from the following equation:[10]

$$m\lambda = n_{active}P(\sin\theta_i + \sin\theta_d) \qquad (3)$$

where n_{active} denotes the refractive index of the P3HT:ICBA, P is the grating period, m specifies the order of the diffracted light, λ is the wavelength of the incident light, and θ_i and θ_d designate the incidence and diffraction angles, respectively. At normal incidence ($\theta_i = 0$), for 350 nm $< \lambda < P$ or $P < \lambda <$ 750 nm (i.e., $P =$ 380, 500, and 650 nm), a diffracted light can have m values of 0, ±1, and ±2 or 0 and ±1, respectively. At higher m values, the θ_d of the diffracted light can be bent by 90°, which cannot be absorbed through the active layer. Actually, although an exact amount of diffracted lights in a backward direction from the active gratings/metal layer in OPVs cannot be directly explored since the photoactive layer absorbs both the front incident and back reflected lights, the diffraction (i.e., diffuse
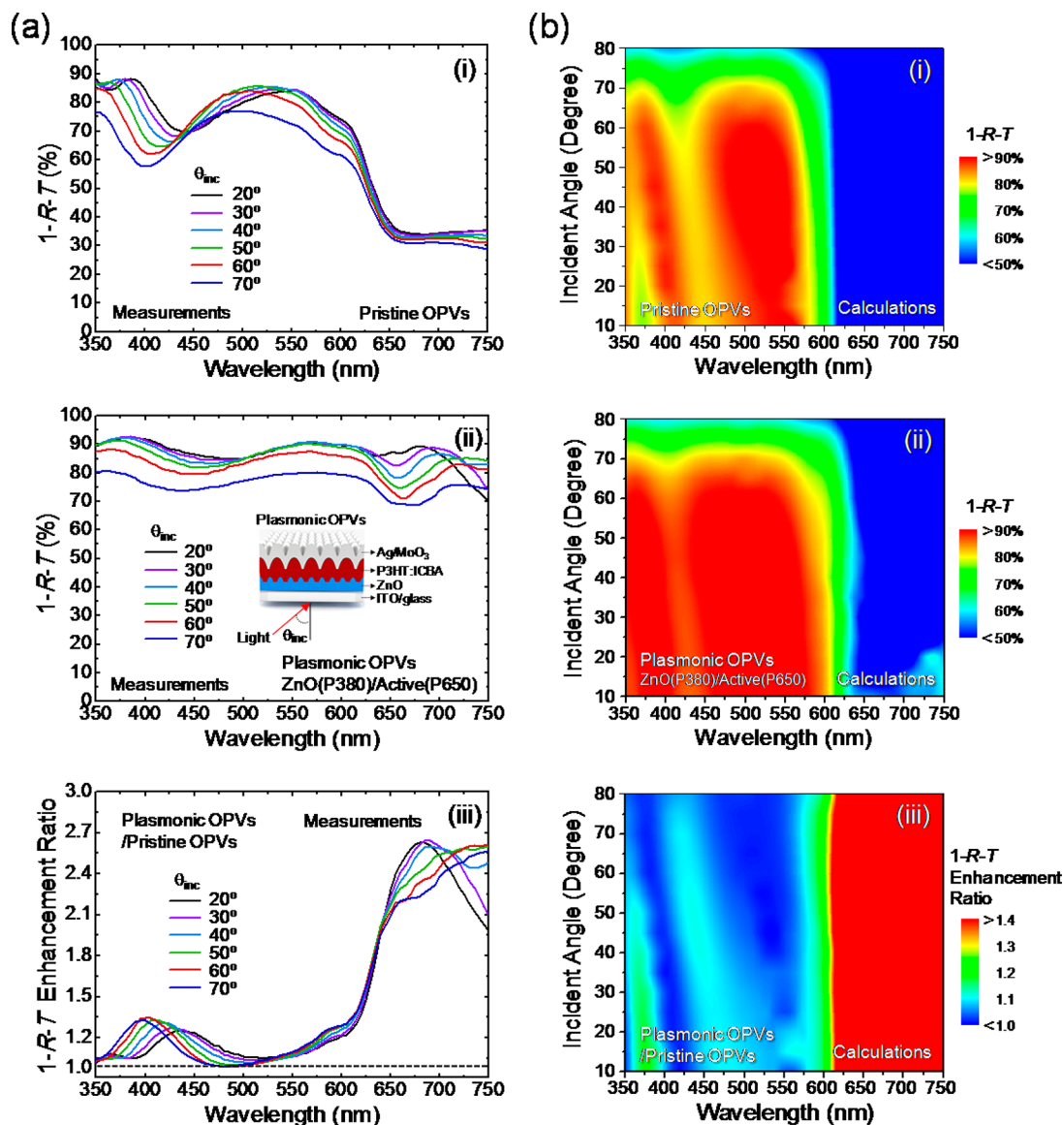
Figure 5. (a) Measured absorption (1-R-T) spectra and (b) contour plots of variations of calculated absorption spectra of (i) pristine OPVs and (ii) plasmonic OPVs with ZnO(P380)/Active(P650) at different incident angles (θ_{inc}). For both the OPVs, the absorption enhancement ratio is also shown in (iii) of (a) and (b), respectively.

light scattering) effect at wavelengths close to the grating period can be found in our previously published papers.[33,34] Our group reported the light-diffraction behaviors of transparent polymers (i.e., Norland Optical Adhesive (NOA) 63 and SU8) with a grating surface, which were prepared by the soft imprint lithography using the same Si master molds and PDMS stamps used in this work. The NOA63 gratings/glass with a period of 650 nm showed a gradual increment in the reflectance spectrum at wavelengths shorter than 650 nm.[33] Similarly, for the gratings on SU8 film/sapphire, a progressive rise in diffuse transmittance spectra toward the wavelengths lower than the grating periods, which were also confirmed in optical theoretical analyses using RCWA simulations, was observed.[34] In this point, considering that the P3HT:ICBA mostly absorbs the incident sunlight in the wavelength region of 350−650 nm, moth-eye active gratings with the period of 650 nm are most suitable for efficient light trapping in plasmonic OPV devices. This relation between the material and period in active gratings of OPVs can be also found in other previous report.[12] In

addition, the diffracted lights reflected from the metal layer can be also recaptured in the active layer due to the total internal reflectance caused by the refractive index (n) contrast between the high-n P3HT:ICBA and low-n ZnO layers (see Figure S3 of Supporting Information).[10] Besides, nanoscale gratings at the interface between the active and metal layers induce the SPRs, exhibiting the enhancement excitation peaks at wavelengths of ∼450 and 670 nm.[11−13] In particular, note that the gratings can effectively capture the light in the active layer though the absorption of the P3HT:ICBA is relatively very low at wavelengths around 670 nm, which enhances the light absorption. At wavelengths close to ∼370 nm, on the other hand, the enhancement is due to the resonant waveguide mode.[11,12] Meanwhile, for the period of 840 nm, the absorption enhancement ratio is relatively lower than that of OPVs with ZnO(P380)/Active(P650). This may be the reason why the number of gratings that can generate the SPR is relatively lower in the same device area though the OPVs with the 840 nm period active gratings have the m values of 0, ±1, ±2, and ±3 at
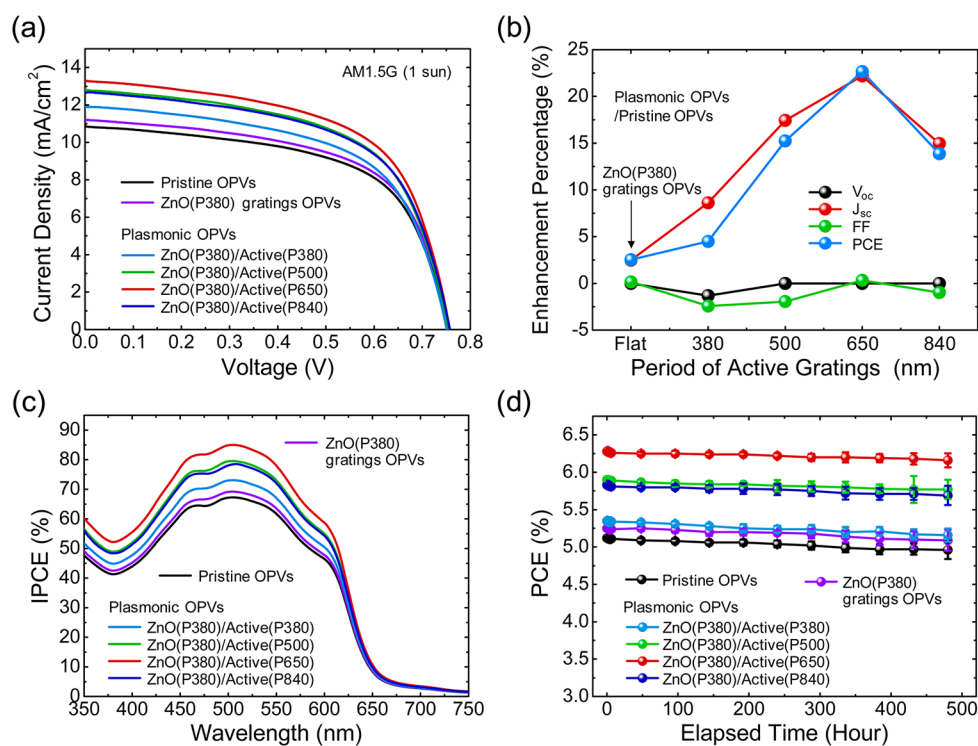
Figure 6. (a) J−V curves, (b) enhancement percentage of device characteristics, (c) IPCE spectra, and (d) stability by elapsed time including the mean and standard deviation values of plasmonic OPVs with active gratings for different periods of 380, 500, 650, and 840 nm at the ZnO (P380) gratings. (a−d) For comparison, the J−V curves, enhancement percentage of device characteristics, IPCE spectra, and stability of pristine OPVs and ZnO (P380) gratings OPVs are also shown.

wavelengths of <500 nm and the interfacial surface area is also reduced compared to the other plasmonic OPVs with active grating periods lower than 840 nm.

To further elucidate the absorption enhancement of OPVs with full moth-eye architectures, their absorption and near-field characteristics were theoretically calculated by the RCWA method. Figure 4 shows the (a) calculated absorption (1-R-T) spectra and enhancement ratio for pristine OPVs and plasmonic OPVs with ZnO(P380)/Active(P650) and (b) near-field intensity distributions in plasmonic OPVs with ZnO(P380)/Active(P650) at different wavelengths of (i) 380 nm, (ii) 460 nm, and (iii) 670 nm for transverse-magnetic (TM) polarized light. As shown in Figure 4a, over an entire wavelength range, the calculated absorption spectra and enhancement ratio results reasonably provide a similar tendency with the measured data in Figure 3c,d. As expected, the absorption spectrum of plasmonic OPVs is higher than that of pristine OPVs in a wide wavelength range of 350−750 nm. The pyramid- or cone-like gratings with gradient effective refractive index profiles in the active layer of photovoltaic cells cause a better optical impedance matching, which can improve the light trapping by the self-enhanced absorption through the coupling of normal incident light adiabatically with laterally scattered light, compared to the planar structure with an abrupt refractive index change.[13] Especially, the significant absorption enhancement occurs at wavelengths around 380, 460, and 670 nm, respectively. These absorption enhancement peaks are relatively well-matched with the measured results, though there is a slight discrepancy due to the difficulty in matching exactly the geometric simulation model to the actual fabricated sample. From the calculated near-field results in Figure 4b, at (i) λ = 380 nm, it can be observed that the TM field is distributed over

the active layer. This is due to the excitation of waveguide mode, which can be characterized by the traveling waves constructively interfering with each other, forming standing waves.[11−13] On the other hand, at (ii) λ = 460 nm in Figure 4b, the SPR occurs in the flat interface (region A) between active and metal (i.e., MoO_3/Ag) layers, together with the excitation of waveguide mode. At (iii) λ = 670 nm, however, the TM fields with a much stronger intensity are distributed at both the flat (region A) and grating sidewall (region B) interfaces between active and metal layers as well as the center (region C) in the active layer over a broad area. At both the regions of A and B, the strong TM-field intensity is attributed to the SPR, while it is caused by the diffracted lights reflected from the rear active/metal gratings at the region C. From these results, the corrugated gratings with periods, which are matched with the absorption edge wavelength of active materials, in the rear electrode (i.e., active/metal layer) can efficiently boost the light absorption in the active layer due to the increase of optical path length and the plasmonic effect as well as the reduced charge-recombination losses, and thus the PCE of OPVs can be considerably improved.

The incident angle of solar irradiance is wide due to the diffused light scattered by the atmosphere and the positional variation of the sun in a day and the seasons. Thus, the incident light angle-dependent optical characteristics of OPV devices are also important. Figure 5 shows the (a) measured absorption (1-R-T) spectra and (b) contour plots of variations of calculated absorption spectra of (i) pristine OPVs and (ii) plasmonic OPVs with ZnO(P380)/Active(P650) at different incident angles (θ_{inc}). For both the OPVs, the absorption enhancement ratio is also shown in (iii) of Figure 5a,b, respectively. As shown in (i) and (ii) of Figure 5a, for both the OPVs, the absorption

spectra were reduced, and their minimum values were slightly shifted toward the shorter-wavelength region in the wavelength range of 350−600 nm when the θ_{inc} is increased from 20 to 70°. As a result, the absorption enhancement peak also moved into the shorter wavelength region with increasing the θ_{inc}, as shown in (iii) of Figure 5a. However, the plasmonic OPVs with ZnO(P380)/Active(P650) exhibited the higher absorption values compared to those of pristine OPVs at each θ_{inc} over a wide wavelength range of 350−750 nm, indicating the higher average A_{sw} value of ∼83.9% at θ_{inc}= 20−70° (i.e., average A_{sw} ≈ 63% for pristine OPVs). In Figure 5b, the calculated absorption results of both the devices also show a similar trend with the measured data, including the absorption enhancement ratio. The angle-dependent absorption characteristics of plasmonic OPVs can be also confirmed in the light-trapping efficiency of Figure S4 (see the Supporting Information). The plasmonic OPVs with ZnO(P380)/Active(P650) show a lower intensity for the reflected light at each θ_{inc}. To compare the quantity of absorption at different θ_{inc} values, the efficiency of light-trapping effect was calculated by the given equation:[26]

$$E = 1 - I_{ref}/I_o \tag{4}$$

where E is the light-trapping efficiency, and I_{ref} and I_o are the intensities of reflected and incident lights, respectively. At θ_{inc}= 15−60°, the plasmonic OPVs had an average light-trapping efficiency of ∼94.4%, which is a much higher value than that (i.e., ∼59.2%) of pristine OPVs. Consequently, the use of gratings on the surfaces of both the front ZnO and rear active layers in OPVs can further improve the solar power generation for the entire day and season.

The effect of ZnO and active gratings on the performance of OPV devices was investigated. Figure 6 shows the (a) J−V curves, (b) enhancement percentage of device characteristics, (c) IPCE spectra, and (d) stability of plasmonic OPVs with active gratings for different periods of 380, 500, 650, and 840 nm at the ZnO (P380) gratings. For comparison, the J−V curves, enhancement percentage of device characteristics, IPCE spectra, and stability of pristine OPVs and OPVs with the only 380 nm period ZnO gratings are also shown in Figure 6a−d. The device characteristics of the corresponding OPVs are summarized in Table 1. For both the pristine and plasmonic OPVs, the open-circuit voltage (V_{oc}) and FF values are generally similar in spite of the electrode with corrugated gratings, which indicates no significant degradation on the electrical properties of the device. On the other hand, the J_{sc}

and PCE values are changed. For the ZnO (P380) gratings OPVs, the slightly increased J_{sc} value of 11.17 mA/cm² was obtained compared to the pristine OPVs (i.e., 10.9 mA/cm²). However, the J_{sc} values of the plasmonic OPVs were significantly enhanced when the gratings were incorporated into the surfaces of front ZnO and rear active layers. In Figure 6b, it can be observed that the PCE enhancement is mainly due to the increased J_{sc}. In particular, the plasmonic OPVs with ZnO(P380)/Active(P650) exhibited the J_{sc} value of 13.32 mA/cm², which is a higher value than those of the other plasmonic OPVs (i.e., J_{sc} ≈ 11.84, 12.8, and 12.53 mA/cm² for periods of 380, 500, and 840 nm in active gratings, respectively), showing a large J_{sc} enhancement percentage of ∼22.2% compared to the pristine OPVs. As a result, an improved PCE of 6.28% was obtained with a considerable PCE enhancement percentage of ∼22.7% compared to the pristine OPVs (i.e., PCE = 5.12%). For the plasmonic OPVs, the increased photocurrents can be also verified in IPCE data of Figure 6c. The plasmonic OPVs with ZnO(P380)/Active(P650) showed a higher IPCE spectrum compared to the other OPV devices over a wide wavelength range of 350−750 nm. This J_{sc} enhancement is attributed to the efficient light-trapping and plasmonic effects as well as the improved photogenerated carrier transport due to the larger interfacial surface area caused by the gratings at surfaces on both the ZnO and active layers in OPVs, as mentioned above.[11−13,24−26] For all the fabricated OPVs, the device performance was also studied for 20 days, as shown in Figure 6d. The performance of all the devices was slightly degraded with increasing the time. Nevertheless, the PCE values of most OPVs were maintained above 95% compared to their initial values during 20 days, which reveals excellent device stability.

4. CONCLUSION

We demonstrated the efficiency enhancement of plasmonic OPVs with a full moth-eye configuration consisting of front ZnO and rear active gratings fabricated by the soft imprint nanopatterning. The introduction of ZnO (P380) and active (P650) gratings into OPVs led to the considerably enhanced photocurrents compared to the pristine OPVs due to the efficient light harvesting, such as the improved light path length, strong light scattering of reflected lights from the metal layer, and SPR effects, and the reduced recombination losses. As a result, the noticeably enhanced PCE of 6.28% was obtained compared to that (i.e., PCE = 5.12%) of the pristine OPVs, exhibiting a PCE enhancement percentage of ∼22.7%. For the angle-dependent absorption characteristics, the plasmonic OPVs had a better performance than those of pristine OPVs. All the OPVs also indicated excellent device stability. Experimental and theoretical results showed that the light-absorption enhancement effect was induced from stronger near-field intensity distributions at the interface between the active and metal layers as well as the center region of active layer. These results have shown that the plasmonic effect has a great potential in applications of OPVs. Also, using the simple and inexpensive fabrication procedure, the proposed full moth-eye architectures can be easily implemented in various organic materials and offer new opportunities in the fabrication of high-performance organic optoelectronic devices for efficient light-harvesting purpose.

Table 1. Device Characteristics of Corresponding OPVs

OPVs[a]	V_{oc} [V]	J_{sc} [mA/cm²]	FF [%]	PCE[b] [%]
pristine	0.76	10.90 ± 0.06	61.8 ± 0.5	5.12 ± 0.04
ZnO(P380)	0.76	11.17 ± 0.08	61.9 ± 0.7	5.25 ± 0.06
ZnO(P380)/ Active(P380)	0.75	11.84 ± 0.16	60.3 ± 1.0	5.35 ± 0.10
ZnO(P380)/ Active(P500)	0.76	12.80 ± 0.15	60.6 ± 0.9	5.90 ± 0.12
ZnO(P380)/ Active(P650)	0.76	13.32 ± 0.12	62.0 ± 0.6	6.28 ± 0.08
ZnO(P380)/ Active(P840)	0.76	12.53 ± 0.15	61.2 ± 0.8	5.83 ± 0.11

[a]For each OPV structure, five devices or more were fabricated in the same fabrication facilities. All the OPV devices were characterized by solar simulator under 1 sun AM1.5G illumination. [b]Mean value ± standard deviation.

■ ASSOCIATED CONTENT

Ⓢ Supporting Information
Cross-sectional view and low-magnification SEM images, optical reflectance and transmittance, angle-dependent light-trapping properties for plasmonic OPVs, including the refractive index and extinction coefficient for the ZnO and P3HT:ICBA. This material is available free of charge via the Internet at http://pubs.acs.org.

■ AUTHOR INFORMATION

Corresponding Authors
*E-mail: eunkim@yonsei.ac.kr. (E.K.)
*E-mail: jsyu@khu.ac.kr. (J.S.Y.)
Author Contributions
§J.W.L. and S.K. contributed equally to this work.
Notes
The authors declare no competing financial interest.

■ ACKNOWLEDGMENTS

■ REFERENCES

(1) Green, M. A.; Emery, K.; Hishikawa, Y.; Warta, W.; Dunlop, E. D. Solar Cell Efficiency Tables (Version 43). *Prog. Photovoltaics* **2014**, *22*, 1−9.
(2) Kaltenbrunner, M.; White, M. S.; Głowacki, E. D.; Sekitani, T.; Someya, T.; Sariciftci, N. S.; Bauer, S. Ultrathin and Lightweight Organic Solar Cells with High Flexibility. *Nat. Commun.* **2012**, *3*, 770.
(3) Eperon, G. E.; Burlakov, V. M.; Goriely, A.; Snaith, H. J. Neutral Color Semitransparent Microstructured Perovskite Solar Cells. *ACS Nano* **2014**, *8*, 591−598.
(4) Li, G.; Zhu, R.; Yang, Y. Polymer Solar Cells. *Nat. Photonics* **2012**, *6*, 153−161.
(5) You, J.; Dou, L.; Yoshimura, K.; Kato, T.; Ohya, K.; Moriarty, T.; Emery, K.; Chen, C. C.; Gao, J.; Li, G.; Yang, Y. A Polymer Tandem Solar Cell with 10.6% Power Conversion Efficiency. *Nat. Commun.* **2013**, *4*, 1446.
(6) Tvingstedt, K.; Persson, N. K.; Inganäs, O.; Rahachou, A.; Zozoulenko, I. V. Surface Plasmon Increase Absorption in Polymer Photovoltaic Cells. *Appl. Phys. Lett.* **2007**, *91*, 113514.
(7) Yang, J.; You, J.; Chen, C. C.; Hsu, W. C.; Tan, H.; Zhang, X. W.; Hong, Z.; Yang, Y. Plasmonic Polymer Tandem Solar Cell. *ACS Nano* **2011**, *5*, 6210−6217.
(8) Monestier, F.; Simon, J. J.; Torchio, P.; Escoubas, L.; Flory, F.; Bailly, S.; Bettignies, R.; Guillerez, S.; Defranoux, C. Modeling the Short-Circuit Current Density of Polymer Solar Cells Based on P3HT:PCBM Blend. *Sol. Energy Mater. Sol. Cells* **2007**, *91*, 405−410.
(9) Li, G.; Shrotriya, V.; Yao, Y.; Yang, Y. Investigation of Annealing Effects and Film Thickness Dependence of Polymer Solar Cells Based on Poly(3-hexylthiophene). *J. Appl. Phys.* **2005**, *98*, 043704.
(10) Na, S. I.; Kim, S. S.; Jo, J.; Oh, S. H.; Kim, J.; Kim, D. Y. Efficient Polymer Solar Cells with Surface Relief Gratings Fabricated by Simple Soft Lithography. *Adv. Funct. Mater.* **2008**, *18*, 3956−3963.
(11) Li, X. H.; Sha, E. I.; Choy, W. C. H.; Fung, D. D. S.; Xie, F. X. Efficient Inverted Polymer Solar Cells with Directly Patterned Active Layer and Silver Back Grating. *J. Phys. Chem. C* **2012**, *116*, 7200−7206.
(12) Li, X.; Choy, W. C. H.; Huo, L.; Xie, F.; Sha, W. E. I.; Ding, B.; Guo, X.; Li, Y.; Hou, J.; You, J.; Yang, Y. Dual Plasmonic

Nanostructures for High Performance Inverted Organic Solar Cells. *Adv. Mater.* **2012**, *24*, 3046−3052.
(13) Chen, J. D.; Zhou, L.; Ou, Q. D.; Li, Y. Q.; Shen, S.; Lee, S. T.; Tang, J. X. Enhanced Light Harvesting in Organic Solar Cells Featuring a Biomimetic Active Layer and a Self-Cleaning Antireflective Coating. *Adv. Energy Mater.* **2014**, *4*, 1301777.
(14) Kim, J.; Koh, J. K.; Kim, B.; Kim, J. H.; Kim, E. Nanopatterning of Mesoporous Inorganic Oxide Films for Efficient Light Harvesting of Dye-Sensitized Solar Cells. *Angew. Chem., Int. Ed.* **2012**, *51*, 6864−6869.
(15) Bi, Y. G.; Feng, J.; Li, Y. F.; Zhang, X. L.; Liu, Y. F.; Jin, Y.; Sun, H. B. Broadband Light Extraction from White Organic Light-Emitting Devices by Employing Corrugated Metallic Electrodes with Dual Periodicity. *Adv. Mater.* **2013**, *25*, 6969−6974.
(16) Bhuvana, T.; Kim, B.; Yang, X.; Shin, H.; Kim, E. Reversible Full-Color Generation with Patterned Yellow Electrochromic Polymers. *Angew. Chem., Int. Ed.* **2013**, *52*, 1180−1184.
(17) Mihi, A.; Beck, F. J.; Lasanta, T.; Rath, A. K.; Konstantatos, G. Imprinted Electrodes for Enhanced Light Trapping in Solution Processed Solar Cells. *Adv. Mater.* **2014**, *26*, 443−448.
(18) Kim, Y.; Yeom, H. R.; Kim, J. Y.; Yang, C. High-Efficiency Polymer Solar Cells with a Cost-Effective Quinoxaline Polymer Through Nanoscale Morphology Control Induced by Practical Processing Additives. *Energy Environ. Sci.* **2013**, *6*, 1909−1916.
(19) Lee, J. K.; Ma, W. L.; Brabec, C. J.; Yuen, J.; Moon, J. S.; Kim, J. Y.; Lee, K.; Bazan, G. C.; Heeger, A. J. Processing Additives for Improved Efficiency from Bulk Heterojunction Solar Cells. *J. Am. Chem. Soc.* **2008**, *130*, 3619−3623.
(20) Leem, J. W.; Kim, S.; Lee, S. H.; Rogers, J. A.; Kim, E.; Yu, J. S. Efficiency Enhancement of Organic Solar Cells Using Hydrophobic Antireflective Inverted Moth-Eye Nanopatterned PDMS Films. *Adv. Energy Mater.* **2014**, *4*, 1301315.
(21) Chen, B.; Zhang, W.; Zhou, X.; Huang, X.; Zhao, X.; Wang, H.; Liu, M.; Lu, Y.; Yang, S. Surface Plasmon Enhancement of Polymer Solar Cells by Penetrating Au/SiO₂ Core/Shell Nanoparticles into All Organic Layers. *Nano Energy* **2013**, *2*, 906−915.
(22) Baek, S. W.; Par, G.; Noh, J.; Cho, C.; Lee, C. H.; Seo, M. K.; Song, H.; Lee, J. Y. Au@Ag Core-Shell Nanocubes for Efficient Plasmonic Light Scattering Effect in Low Bandgap Organic Solar Cells. *ACS Nano* **2014**, *8*, 3302−3312.
(23) Xu, Y.; Munday, J. N. Light Trapping in a Polymer Solar Cell by Tailored Quantum Dot Emission. *Opt. Express* **2014**, *22*, A259−A267.
(24) Wang, D. H.; Choi, D. G.; Lee, K. J.; Jeong, J. H.; Jeon, S. H.; Park, O. O.; Park, J. H. Effect of the Ordered 2D-Dot Nano-Patterned Anode for Polymer Solar Cells. *Org. Electron.* **2010**, *11*, 285−290.
(25) Ham, J.; Lee, J. L. ITO Breakers: Highly Transparent Conducting Polymer/Metal/Dielectric (P/M/D) Films for Organic Solar Cells. *Adv. Energy Mater.* **2014**, *4*, 1400539.
(26) Kim, S.; Koh, J. H.; Yang, X.; Chi, W. S.; Park, C.; Leem, J. W.; Kim, B.; Seo, S.; Kim, Y.; Yu, J. S.; Kim, J. H.; Kim, E. Enhanced Device Efficiency of Bilayered Inverted Organic Solar Cells Based on Photocurable P3HTs with a Light-Harvesting ZnO Nanorod Array. *Adv. Energy Mater.* **2014**, *4*, 1301338.
(27) Jin, Y.; Feng, J.; Xu, M.; Zhang, X. L.; Wang, L.; Chen, Q. D.; Wang, H. Y.; Sun, H. B. Matching Photocurrents of Sub-cells in Double-Junction Organic Solar Cells via Coupling Between Surface Plasmon Polaritons and Microcavity Modes. *Adv. Optical Mater.* **2013**, *1*, 809−813.
(28) Leem, J. W.; Song, Y. M.; Yu, J. S. Biomimetic Artificial Si Compound Eye Surface Structures with Broadband and Wide-angle Antireflection Properties for Si-Based Optoelectronic Applications. *Nanoscale* **2013**, *5*, 10455−10460.
(29) Leem, J. W.; Yeh, Y.; Yu, J. S. Enhanced Transmittance and Hydrophilicity of Nanostructured Glass Substrates with Antireflective Properties Using Disordered Gold Nanopatterns. *Opt. Express* **2012**, *20*, 4056−4066.
(30) Sun, Y.; Seo, J. H.; Takacs, C. J.; Seifter, J.; Heeger, A. J. Inverted Polymer Solar Cells Integrated with a Low-Temperature-

Annealed Sol-Gel-Derived ZnO Film as an Electron Transport Layer. *Adv. Mater.* **2011**, *23*, 1679−1683.

(31) Leem, J. W.; Song, Y. M.; Lee, Y. T.; Yu, J. S. Effect of Etching Parameters on Antireflection Properties of Si Subwavelength Grating Structures for Solar Cell Applications. *Appl. Phys. B: Laser Opt.* **2010**, *100*, 891−896.

(32) Song, Y. M.; Choi, H. J.; Yu, J. S.; Lee, Y. T. Design of Highly Transparent Glasses with Broadband Antireflective Subwavelength Structures. *Opt. Express* **2010**, *18*, 13063−13071.

(33) Leem, J. W.; Guan, X. Y.; Choi, M.; Yu, J. S. Broadband and Omnidirectional Highly-Transparent Coverglasses Coated with Biomimetic Moth-Eye Nanopatterned Polymer Films for Solar Photovoltaic System Applications. *Sol. Energy Mater. Sol. Cells* **2015**, *134*, 45−53.

(34) Lee, S. H.; Leem, J. W.; Yu, J. S. Transmittance Enhancement of Sapphires with Antireflective Subwavelength Grating Patterned UV Polymer Surface Structures by Soft Lithography. *Opt. Express* **2013**, *21*, 29298−29303.

(35) Clapham, P. B.; Hutley, M. C. Reduction of Lens Reflexion by the 'Moth Eye' Principle. *Nature* **1973**, *244*, 281−282.

(36) Stavenga, D. G.; Foletti, S.; Palasantzas, G.; Arikawa, K. Light on the Moth-Eye Corneal Nipple Array of Butterflies. *Proc. R. Soc. London, Ser. B* **2006**, *273*, 661−667.

(37) NREL's Renewable Resource Data Center. http://rredc.nrel.gov/solar/spectra/am1.5; accessed May 1, 2014.

(38) Meysing, D. M.; Burst, J. M.; Rance, W. L.; Reese, M. O.; Barnes, T. M.; Gessert, T. A.; Wolden, C. A. The Influence of Cadmium Sulfide and Contact Annealing Configuration on the Properties of High-Performance Cadmium Stannate. *Sol. Energy Mater. Sol. Cells* **2013**, *117*, 300−305.

(39) Emah, J. B.; Curry, R. J.; Silva, S. R. P. Low Cost Patterning of Poly(3,4-ethylenedioxythiophene)poly(tyrenesulfonate) Films to Increase Organic Photovoltaic Device Efficiency. *Appl. Phys. Lett.* **2008**, *93*, 103301.

(40) Min, C.; Li, J.; Veronis, G.; Lee, J. Y.; Fan, S.; Peumans, P. Enhancement of Optical Absorption in Thin-Film Organic Solar Cells Through the Excitation of Plasmonic Modes in Metallic Gratings. *Appl. Phys. Lett.* **2010**, *96*, 133302.

(41) Leem, J. W.; Kim, Y. P.; Yu, J. S. Tunable Behavior of Reflectance Minima in Periodic Ge Submicron Grating Structures. *J. Opt. Soc. Am. B* **2012**, *29*, 357−362.